

# Active Disturbance Rejection Control for MEMS Gyroscopes<sup>1</sup>

Qing Zheng<sup>2</sup>, *Student Member, IEEE*, Lili Dong<sup>2,\*</sup>, *Member, IEEE*, Dae Hui Lee<sup>2</sup>, Zhiqiang Gao<sup>2</sup>, *Member, IEEE*

**Abstract**— A new control method is presented to drive the drive axis of a MEMS gyroscope to resonance and regulate the output amplitude of the axis to a fixed level. It is based on a unique active disturbance rejection control (ADRC) strategy, which actively estimates and compensates for internal dynamic changes of the plant and external disturbances in real time. The stability analysis shows that both the estimation error and the tracking error of the drive axis output are bounded and the upper bounds of the errors monotonously decrease with the bandwidths. The control system is simulated and tested using a field programmable gate array (FPGA)-based digital implementation on a piezoelectric vibration gyroscope. Both simulation and experimental results demonstrate that the proposed control method not only drives the drive axis to vibrate along the desired trajectory but also compensates for manufacture imperfections in a robust fashion that is insensitive to parameter variations and noises.

**Keywords:** MEMS gyroscopes, extended state observer, active disturbance rejection control, FPGA.

## I. INTRODUCTION

MEMS (micro-electro-mechanical systems) gyroscope is a micro-scaled or millimeter-scaled inertial rate sensor. It has been applied to automotives (stability control and GPS), aerospace (GPS assisted inertial navigation), and consumer electronics (camera image stabilization and 3-dimensional mouse) [1]. Compared to electro-mechanical gyroscopes, the MEMS gyroscope is small in size, inexpensive, and energy-efficient. A control system is generally used to excite the vibration along two vibrating modes (driving and sensing modes) of the MEMS gyroscope and to estimate the rotation rate. However, the small size of the MEMS gyroscope puts a big challenge on controller design and micro-fabrication. The imprecise micro-fabrications and surrounding disturbances result in mechanical coupling terms between two axes, mechanical-thermal noises, and parameter variations, and consequently degrade the performance of the MEMS gyroscope. Therefore, a closed-loop control system is essential for improving the performance of the MEMS gyroscope through effectively compensating for the mechanical imperfections and the disturbances in control efforts.

Since the 1990s, there has been a limited amount of research on the feedback control system designs of the MEMS gyroscopes. The controllers introduced in [2-4]

disregard the mechanical coupling terms on the drive axis caused by the manufacture imperfections. The adaptive controllers in [5, 6] neglect the noises. The adaptive controller in [7] is designed for the MEMS gyroscopes operating in adaptive mode. However, most reported MEMS gyroscopes operate in conventional mode [8] where the movement of the mass along the drive axis is relatively large and the movement along the sense axis is very small. The controller in [8] controls the vibrating along the sensing mode of the MEMS gyroscope while the control of driving mode is disregarded.

In this paper, a practical solution based on the active disturbance rejection control (ADRC) technology is applied to the driving mode of the conventional MEMS gyroscope [9-10]. The ADRC has been successfully employed in many mechanical systems [11-14]. The basic idea of this control strategy is to estimate the plant dynamics and disturbances using an extended state observer (ESO) and to actively compensate for the disturbance in control effort. With the accurate estimation of the plant dynamics and disturbances by ESO, the ADRC is very robust against parameter variations, disturbances, and noise. To test the effectiveness of the ADRC, a field programmable gate array (FPGA)-based digital implementation is conducted on a vibrational beam gyroscope. The experimental results demonstrate the feasibility of the controller.

This paper is organized as follows: The dynamics of MEMS gyroscopes is described in Section II. The ADRC approach and its stability analysis are presented in Section III. Software simulation and hardware test results are shown in Section IV. The paper ends with a few concluding remarks in Section V.

## II. DYNAMICS OF MEMS GYROSCOPES

The mechanical structure of the MEMS gyroscope can be understood as a proof mass attached to a rigid frame by springs and dampers as shown in Fig. 1. As the mass is driven to resonance along the drive (X) axis and the rigid frame is rotating along the rotation axis, a Coriolis acceleration will be produced along the sense (Y) axis, which is perpendicular to both drive and rotation axes. The Coriolis acceleration is proportional to the amplitude of the output of the drive axis and the unknown rotation rate [1]. Therefore, we can estimate the rotation rate through sensing the vibration of the sense axis. In order to accurately sense the rotation rate, the vibration magnitude of the drive axis has to be regulated to a fixed level. Therefore, the controller of the drive axis is mainly used to drive the drive axis to resonance, and to regulate the output amplitude.

<sup>1</sup>The work is supported by Ohio ICE (Instrumental, Control, and Electronic) consortium under grant 0260-0652-10.

<sup>2</sup>The authors are with the Department of Electrical and Computer Engineering at Cleveland State University, Cleveland, OH 44115.

\*Corresponding author. Email: L.Dong34@csuohio.edu.

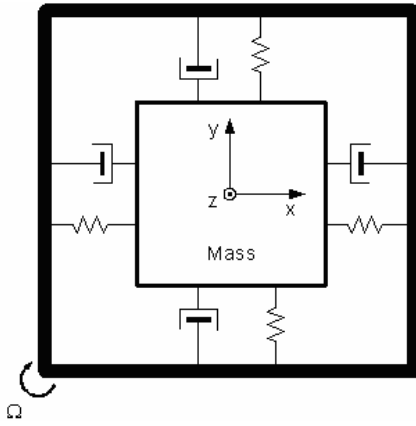


Fig. 1 Mass-spring-damper structure of MEMS gyroscopes.

Assuming the natural frequencies of both axes are the same, the vibrational MEMS gyroscope is modeled as

$$\begin{aligned} \ddot{x} + 2\zeta\omega_n\dot{x} + \omega_n^2x + \omega_{xy}y - 2\Omega\dot{y} &= \frac{k}{m}u_d \\ \ddot{y} + 2\zeta\omega_n\dot{y} + \omega_n^2y + \omega_{xy}x + 2\Omega\dot{x} &= \frac{1}{m}N(t) \end{aligned} \quad (1)$$

where  $x$  and  $y$  are the outputs of the drive and sense axes,  $2\Omega\dot{x}$  and  $2\Omega\dot{y}$  are the Coriolis accelerations,  $\Omega$  is the rotation rate,  $\omega_n$  is the natural frequency of the drive and sense axes,  $\omega_{xy}y$  and  $\omega_{yx}x$  are Quadrature errors caused by spring couplings between two axes,  $\zeta$  is the damping coefficient,  $m$  is the mass of the MEMS gyroscope,  $k$  is the controller gain, and  $u_d$  is the control input for drive axis. In (1), mechanical thermal noise on the sense axis is represented by the random force  $N(t)$ . The effects of thermal noise on the drive axis are negligible and are ignored [15]. In the MEMS gyroscopes represented by (1), the Quadrature errors are unknown signals, the rotation rate  $\Omega$  is unknown, and the damping coefficient typically has a large varying range. In this paper, we assume the sense axis is working under the open-loop operation. Our control objective is to force the drive axis to oscillate at specified amplitude and resonant frequency in the presence of parameter uncertainties, mechanical couplings, and mechanical-thermal noises.

### III. ACTIVE DISTURBANCE REJECTION CONTROL

In this paper, ADRC is employed to control MEMS gyroscopes by dealing with modeling errors and structural uncertainties. In particular, an ESO provides an estimate of the internal dynamics of the MEMS gyroscope and the external disturbances which include the output disturbances, the unknown time varying rotation rate, and the unknown Quadrature error terms arising from mechanical imperfections. With the dynamic compensation of the estimated information, the plant is reduced to a double integrator. Then a PD controller is sufficient to control it.

Both the drive and sense axes of MEMS gyroscopes can be taken as lightly damped second-order systems. We can rewrite the drive axis model in (1) as

$$\ddot{x} = f(x, \dot{x}, d) + bu_d \quad (2)$$

where  $u_d$  is the control signal of the drive axis,  $b=k/m$ ,  $d$  is the external disturbance,  $f(x, \dot{x}, d)$ , or simply denoted as  $f$ , represents both the internal dynamics and the external disturbance, and

$$f = -2\zeta\omega_n\dot{x} - \omega_n^2x - \omega_{xy}y + 2\Omega\dot{y}. \quad (3)$$

The basic idea of ADRC is to obtain the estimated  $f$ , i.e.,  $\hat{f}$ , in real time by an ESO, and to actively compensate for it in the control law. The concept of ADRC is introduced as follows.

#### A. Extended State Observer Design

$$\text{Let } \xi_1 = x, \xi_2 = \dot{x}, \xi_3 = f \text{ and } \xi = [\xi_1 \ \xi_2 \ \xi_3]^T.$$

Assuming  $f$  is differentiable, the state space form of (2) is

$$\begin{cases} \dot{\xi} = A\xi + Bu_d + Eh \\ x = C\xi \end{cases} \quad (4)$$

$$\text{where } A = \begin{bmatrix} 0 & 1 & 0 \\ 0 & 0 & 1 \\ 0 & 0 & 0 \end{bmatrix}, B = \begin{bmatrix} 0 \\ b \\ 0 \end{bmatrix}, C = [1 \ 0 \ 0], E = \begin{bmatrix} 0 \\ 0 \\ 1 \end{bmatrix}.$$

Note that  $\xi_3 = f$  is the augmented state and  $h = \dot{f}$ . A continuous ESO for (4) is designed as

$$\begin{cases} \dot{\hat{\xi}} = A\hat{\xi} + Bu_d + L(x - \hat{x}) \\ \hat{x} = C\hat{\xi} \end{cases} \quad (5)$$

where  $L = [l_1 \ l_2 \ l_3]^T$  is the observer gain. The observer gains are chosen such that the characteristic polynomial  $s^3 + l_1s^2 + l_2s + l_3$  is Hurwitz. For tuning simplicity, all the observer poles are placed at  $-\omega_o$ . It results in the characteristic polynomial of (5) to be

$$\lambda_o(s) = s^3 + l_1s^2 + l_2s + l_3 = (s + \omega_o)^3 \quad (6)$$

where  $\omega_o$  is the observer bandwidth of the drive axis and  $L = [3\omega_o \ 3\omega_o^3 \ \omega_o^3]^T$ .

#### B. Control Algorithm

Once the observer is designed and well tuned, its outputs will track  $\xi_1$ ,  $\xi_2$ , and  $\xi_3$  respectively. By canceling the effect of  $f$  using  $\hat{\xi}_3$ , ADRC actively compensates for  $f$  in real time.

The ADRC control law is given by

$$u_d = \frac{k_1(r - \hat{\xi}_1) + k_2(\dot{r} - \hat{\xi}_2) - \hat{\xi}_3 + \ddot{r}}{b} \quad (7)$$

where  $r$  is the desired trajectory of the drive axis,  $k_1$  and  $k_2$  are the controller gain parameters selected to make  $s^2 + k_2s + k_1$  Hurwitz. For simplicity, let  $k_1 = \omega_c^2$ ,  $k_2 = 2\omega_c$ , where  $\omega_c$  is the controller bandwidth. The closed-loop system for the drive axis becomes

$$\ddot{x} = (f - \hat{\xi}_3) + k_1(r - \hat{\xi}_1) + k_2(\dot{r} - \hat{\xi}_2) + \ddot{r}. \quad (8)$$

Note that with a well-designed ESO, the first term in the right hand side (RHS) of (8) is negligible and the rest of the terms in the RHS of (8) constitutes a PD controller with a feedforward term. The convergence for the estimation error

of the ESO and the closed-loop tracking error of ADRC is shown below.

### C. Stability

#### 1) Convergence of the ESO

Let  $\tilde{\xi}_i(t) = \xi_i(t) - \hat{\xi}_i(t)$ ,  $i = 1, 2, 3$ . From (4) and (5), the observer estimation error dynamics can be shown as

$$\begin{aligned}\dot{\tilde{\xi}}_1 &= \tilde{\xi}_2 - l_1 \tilde{\xi}_1 \\ \dot{\tilde{\xi}}_2 &= \tilde{\xi}_3 - l_2 \tilde{\xi}_1 \\ \dot{\tilde{\xi}}_3 &= h - l_3 \tilde{\xi}_1.\end{aligned}\quad (9)$$

Now let us scale the observer estimation error  $\tilde{\xi}_i(t)$  by  $\omega_o^{i-1}$ , i.e., let  $\varepsilon_i(t) = \frac{\tilde{\xi}_i(t)}{\omega_o^{i-1}}$ ,  $i = 1, 2, 3$ . Then (9) can be rewritten as

$$\dot{\varepsilon} = \omega_o A_\varepsilon \varepsilon + B_\varepsilon \frac{h(\xi, d)}{\omega_o^2} \quad (10)$$

$$\text{where } A_\varepsilon = \begin{bmatrix} -3 & 1 & 0 \\ -3 & 0 & 1 \\ -1 & 0 & 0 \end{bmatrix}, B_\varepsilon = \begin{bmatrix} 0 \\ 0 \\ 1 \end{bmatrix}.$$

*Theorem 1:* Assuming  $h(\xi, d)$  is bounded, then there exist a constant  $\sigma_i > 0$  and a finite time  $T_1 > 0$  such that  $|\tilde{\xi}_i(t)| \leq \sigma_i$ ,  $i = 1, 2, 3$ ,  $\forall t \geq T_1 > 0$  and  $\omega_o > 0$ . Furthermore,

$$\sigma_i = O\left(\frac{1}{\omega_o^k}\right), \text{ for some positive integer } k.$$

*Proof:* Solving (10), we can obtain

$$\varepsilon(t) = e^{\omega_o A_\varepsilon t} \varepsilon(0) + \int_0^t e^{\omega_o A_\varepsilon (t-\tau)} B_\varepsilon \frac{h(\xi(\tau), d)}{\omega_o^2} d\tau. \quad (11)$$

Let

$$p(t) = \int_0^t e^{\omega_o A_\varepsilon (t-\tau)} B_\varepsilon \frac{h(\xi(\tau), d)}{\omega_o^2} d\tau. \quad (12)$$

Since  $h(\xi(\tau), d)$  is bounded, that is,  $|h(\xi(\tau), d)| \leq \delta$ , where  $\delta$  is a positive constant, it follows that

$$|p_i(t)| \leq \frac{\delta}{\omega_o^3} \left[ |(A_\varepsilon^{-1} B_\varepsilon)_i| + |(A_\varepsilon^{-1} e^{\omega_o A_\varepsilon t} B_\varepsilon)_i| \right] \quad (13)$$

for  $i = 1, 2, 3$ . Since  $A_\varepsilon^{-1} = \begin{bmatrix} 0 & 0 & -1 \\ 1 & 0 & -3 \\ 0 & 1 & -3 \end{bmatrix}$ , One has

$$\left| (A_\varepsilon^{-1} B)_i \right| = \begin{cases} 1 \\ 3 \\ 3 \end{cases}_{i=1,2,3}. \quad (14)$$

Since  $A_\varepsilon$  is Hurwitz, there exists a finite time  $T_1 > 0$  such that

$$\left| \left[ e^{\omega_o A_\varepsilon t} \right]_{ij} \right| \leq \frac{1}{\omega_o^3} \quad (15)$$

for all  $t \geq T_1$ ,  $i, j = 1, 2, 3$ . Hence

$$\left| \left[ e^{\omega_o A_\varepsilon t} B \right]_i \right| \leq \frac{1}{\omega_o^3} \quad (16)$$

for all  $t \geq T_1$ ,  $i = 1, 2, 3$ . Note that  $T_1$  depends on  $\omega_o A_\varepsilon$ .

Let  $A_\varepsilon^{-1} = \begin{bmatrix} s_{11} & s_{12} & s_{13} \\ s_{21} & s_{22} & s_{23} \\ s_{31} & s_{32} & s_{33} \end{bmatrix}$  and

$$e^{\omega_o A_\varepsilon t} = \begin{bmatrix} d_{11} & d_{12} & d_{13} \\ d_{21} & d_{22} & d_{23} \\ d_{31} & d_{32} & d_{33} \end{bmatrix}. \text{ One has}$$

$$\left| \left( A_\varepsilon^{-1} e^{\omega_o A_\varepsilon t} B_\varepsilon \right)_i \right| \leq \begin{cases} \frac{1}{\omega_o^3} \\ \frac{4}{\omega_o^3} \end{cases}_{i=1,2,3} \quad (17)$$

for all  $t \geq T_1$ . From (13), (14) and (17), we obtain

$$|p_i(t)| \leq \frac{\delta}{\omega_o^3} \left[ 3 + \frac{4}{\omega_o^3} \right] = \frac{3\delta}{\omega_o^3} + \frac{4\delta}{\omega_o^6} \quad (18)$$

for all  $t \geq T_1$ ,  $i = 1, 2, 3$ . Let  $\varepsilon_{sum}(0) = |\varepsilon_1(0)| + |\varepsilon_2(0)| + |\varepsilon_3(0)|$ . It follows that

$$\left| \left[ e^{\omega_o A_\varepsilon t} \varepsilon(0) \right]_i \right| \leq \frac{\varepsilon_{sum}(0)}{\omega_o^3} \quad (19)$$

for all  $t \geq T_1$ ,  $i = 1, 2, 3$ . From (11), one has

$$|\varepsilon_i(t)| \leq \left| \left[ e^{\omega_o A_\varepsilon t} \varepsilon(0) \right]_i \right| + |p_i(t)|. \quad (20)$$

Let  $\tilde{\xi}_{sum}(0) = |\tilde{\xi}_1(0)| + |\tilde{\xi}_2(0)| + |\tilde{\xi}_3(0)|$ . According to

$\varepsilon_i(t) = \frac{\tilde{\xi}_i(t)}{\omega_o^{i-1}}$  and (18)-(20), we have

$$\begin{aligned} |\tilde{\xi}_i(t)| &\leq \left| \frac{\tilde{\xi}_{sum}(0)}{\omega_o^3} \right| + \frac{3\delta}{\omega_o^{4-i}} + \frac{4\delta}{\omega_o^{7-i}} \\ &= \sigma_i \end{aligned} \quad (21)$$

for all  $t \geq T_1$ ,  $i = 1, 2, 3$ . Q.E.D.

It has been proven above that in the absence of the plant model, the estimation error of the ESO (5) is bounded and its upper bound monotonously decreases with the observer bandwidth. The convergence of ADRC, where ESO is employed, is analyzed next.

#### 2) Convergence of the ADRC

Let  $[r_1, r_2, r_3]^T = [r, \dot{r}, \ddot{r}]^T$  and  $e_i(t) = r_i(t) - \xi_i(t)$ ,  $i = 1, 2$ .

*Theorem 2:* Assuming that  $h$  is bounded, there exist a constant  $\rho_i > 0$  and a finite time  $T_3 > 0$  such that  $|e_i(t)| \leq \rho_i$ ,  $i = 1, 2$ ,  $\forall t \geq T_3 > 0$ ,  $\omega_o > 0$  and  $\omega_c > 0$ .

Furthermore,  $\rho_i = O\left(\frac{1}{\omega_c^q}\right)$  for some positive integer  $q$ .

*Proof:* From (7), one has

$$u_d = \frac{k_1(e_1 + \tilde{\xi}_1) + k_2(e_2 + \tilde{\xi}_2) - (\xi_3 - \tilde{\xi}_3) + r_3}{b}. \quad (22)$$

It follows that

$$\begin{aligned} \dot{e}_1 &= \dot{r}_1 - \dot{\xi}_1 = r_2 - \xi_2 = e_2 \\ \dot{e}_2 &= -k_1(e_1 + \tilde{\xi}_1) - k_2(e_2 + \tilde{\xi}_2) - \tilde{\xi}_3. \end{aligned} \quad (23)$$

Let  $e(t) = [e_1(t), e_2(t)]^T$ ,  $\tilde{\xi}(t) = [\tilde{\xi}_1(t), \tilde{\xi}_2(t), \tilde{\xi}_3(t)]^T$ , then

$$\dot{e}(t) = A_e e(t) + A_{\tilde{\xi}} \tilde{\xi}(t) \quad (24)$$

$$\text{where } A_e = \begin{bmatrix} 0 & 1 \\ -k_1 & -k_2 \end{bmatrix} \text{ and } A_{\tilde{\xi}} = \begin{bmatrix} 0 & 0 & 0 \\ -k_1 & -k_2 & -1 \end{bmatrix}.$$

Solving (24), we have

$$e(t) = e^{A_e t} e(0) + \int_0^t e^{A_e(t-\tau)} A_{\tilde{\xi}} \tilde{\xi}(\tau) d\tau. \quad (25)$$

According to (24) and Theorem 1, one has

$$\begin{aligned} [A_{\tilde{\xi}} \tilde{\xi}(\tau)]_{i=1} &= 0 \\ [A_{\tilde{\xi}} \tilde{\xi}(\tau)]_2 &= |-k_1 \tilde{\xi}_1(\tau) - k_2 \tilde{\xi}_2(\tau) - \tilde{\xi}_3(\tau)| \\ &\leq k_{sum} \sigma_i = \gamma \text{ for all } t \geq T_1 \end{aligned} \quad (26)$$

where  $k_{sum} = 1 + k_1 + k_2$ . Let  $\varphi(t) = \int_0^t e^{A_e(t-\tau)} A_{\tilde{\xi}} \tilde{\xi}(\tau) d\tau$ .

Define  $\Psi = [0 \ \gamma]^T$ . It follows that

$$|\varphi_i(t)| \leq |(A_e^{-1} \Psi)_i| + |(A_e^{-1} e^{A_e t} \Psi)_i|. \quad (27)$$

Since  $A_e^{-1} = \begin{bmatrix} -\frac{k_2}{k_1} & -\frac{1}{k_1} \\ 1 & 0 \end{bmatrix} = \begin{bmatrix} -\frac{2}{\omega_c} & -\frac{1}{\omega_c^2} \\ 1 & 0 \end{bmatrix}$ , we have

$$\begin{aligned} |(A_e^{-1} \Psi)_1| &= \frac{\gamma}{\omega_c^2} \\ |(A_e^{-1} \Psi)_2| &= 0. \end{aligned} \quad (28)$$

Since  $A_e$  is Hurwitz, there exists a finite time  $T_2 > 0$  such that

$$\left| [e^{A_e t}]_{ij} \right| \leq \frac{1}{\omega_c^3} \quad (29)$$

for all  $t \geq T_2$ ,  $i, j = 1, 2$ . Note that  $T_2$  depends on  $A_e$ . Let

$$e^{A_e t} = \begin{bmatrix} o_{11} & o_{12} \\ o_{21} & o_{22} \end{bmatrix} \text{ and } e_{sum}(0) = |e_1(0)| + |e_2(0)|. \text{ It follows}$$

that

$$\left| [e^{A_e t} e(0)]_i \right| \leq \frac{e_{sum}(0)}{\omega_c^3} \quad (30)$$

for all  $t \geq T_2$ ,  $i = 1, 2$ . Let  $T_3 = \max\{T_1, T_2\}$ . We have

$$\left| (e^{A_e t} \Psi)_i \right| \leq \frac{\gamma}{\omega_c^3} \quad (31)$$

for all  $t \geq T_3$ ,  $i = 1, 2$ , and

$$\left| (A_e^{-1} e^{A_e t} \Psi)_i \right| \leq \begin{cases} \frac{1+2\omega_c}{\omega_c^2} \frac{\gamma}{\omega_c^3} \Big|_{i=1} \\ \frac{\gamma}{\omega_c^3} \Big|_{i=2} \end{cases} \quad (32)$$

for all  $t \geq T_3$ . From (27), (28), and (32), we obtain

$$|\varphi_i(t)| \leq \begin{cases} \frac{\gamma}{\omega_c^2} + \frac{1+2\omega_c}{\omega_c^2} \frac{\gamma}{\omega_c^3} \Big|_{i=1} \\ \frac{\gamma}{\omega_c^3} \Big|_{i=2} \end{cases} \quad (33)$$

for all  $t \geq T_3$ . From (25), one has

$$|e_i(t)| \leq \left| [e^{A_e t} e(0)]_i \right| + |\varphi_i(t)|. \quad (34)$$

According to (30), (33)-(34), we have

$$|e_i(t)| \leq \begin{cases} \frac{e_{sum}(0)}{\omega_c^3} + \frac{(1+2\omega_c + \omega_c^2)\sigma_i}{\omega_c^2} + \frac{(1+2\omega_c + \omega_c^2)(1+2\omega_c)\sigma_i}{\omega_c^5} \Big|_{i=1} \\ \frac{e_{sum}(0) + (1+2\omega_c + \omega_c^2)\sigma_i}{\omega_c^3} \Big|_{i=2} \end{cases} \leq \rho_i \quad (35)$$

for  $t \geq T_3$ ,  $i = 1, 2$ , where

$$\rho_i = \max \left\{ \frac{e_{sum}(0)}{\omega_c^3} + \frac{(1+2\omega_c + \omega_c^2)\sigma_i}{\omega_c^2}, \frac{(1+2\omega_c + \omega_c^2)(1+2\omega_c)\sigma_i}{\omega_c^5}, \frac{e_{sum}(0) + (1+2\omega_c + \omega_c^2)\sigma_i}{\omega_c^3} \right\}.$$

Q.E.D.

It has been shown above that, with plant dynamics largely unknown, the tracking error and its derivative of ADRC are bounded and their upper bounds monotonously decrease with the controller bandwidth. With the convergence of ESO and ADRC established, we now present the simulation and hardware test results.

#### IV. SIMULATION AND HARDWARE TESTS

An FPGA-based digital implementation of the ADRC is designed and conducted on an experimentally used vibrational beam gyroscope. The control algorithm is implemented in custom logic using VHDL.

##### A. Hardware Setup

The block diagram of the FPGA-based digital implementation is shown in Fig. 2. The hardware setup includes a core hardware board developed earlier as reconfigurable control and communication module (RCCM) [14]. It mainly consists of two analog to digital converters (ADC), each preceded by an analog programmable filter, Flash memory and an FPGA chip. The RCCM also supports the Ethernet and controller area network (CAN) communication. In this implementation, the sinusoidal reference signal, the Nios core processor, and first input first output (FIFO) buffer are programmed into the FPGA circuit. The control algorithm, ADRC, is also programmed into FPGA using the VHDL language. One external 12-bit digital to analog converter (DAC) is employed to convert the digital control signal from FPGA to analog form before it enters the gyroscope circuitry. To close the loop, the output of the gyroscope is first amplified and then fed to the field programmable analog array (FPAA) chip on RCCM. In the control system design, ADRC employs very large controller and observer gains, which is beyond the limited range of

integer numbers represented by 32-bit binary. For this reason, the single precision floating-point from IEEE standard 754 is used for the FPGA-based ADRC design.

In terms of development tools, Quartus II, version 3.2, for FPGA design, SOPC builder for Nios embedded processor design, and GNUPro compiler for building both software and libraries, are employed.

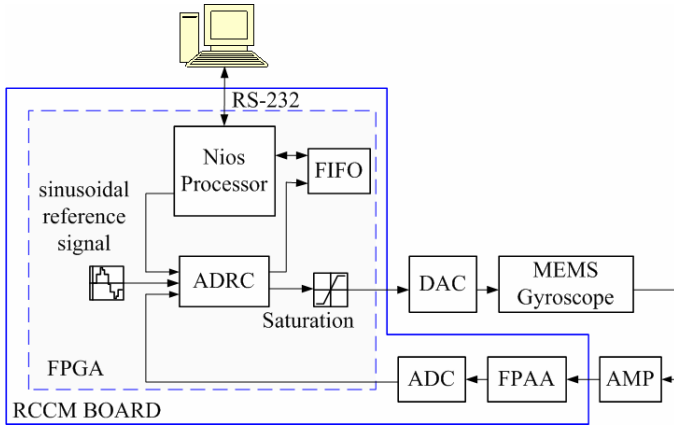


Fig. 2 The control system for the MEMS gyroscope.

### B. FPGA Implementation of the ADRC

For digital implementation, discretizing the state space model (4) using zero-order hold (ZOH) by ignoring  $h$ , we have

$$\begin{cases} \xi(k+1) = \Phi \xi(k) + \Gamma u_d(k) \\ x(k) = H \xi(k) \end{cases} \quad (36)$$

where

$$\Phi = e^{AT_s} = \begin{bmatrix} 1 & T_s & \frac{T_s^2}{2} \\ 0 & 1 & T_s \\ 0 & 0 & 1 \end{bmatrix}, \Gamma = \int_0^{T_s} e^{A\eta} d\eta B = \begin{bmatrix} \frac{T_s^2 b}{2} \\ T_s b \\ 0 \end{bmatrix}, H = [1 \quad 0 \quad 0],$$

and  $T_s$  is the sampling period.

A discrete ESO is designed as [16]

$$\hat{\xi}(k) = \bar{\xi}(k) + L_c [x(k) - H\bar{\xi}(k)] \quad (37)$$

where  $L_c$  is the estimator gain,  $\hat{\xi}(k)$  provides a current estimate of  $\xi(k)$  based on the current measurement  $x(k)$ , and  $\bar{\xi}(k)$  is the predicted estimate based on a prediction from the previous time estimate, that is

$$\bar{\xi}(k) = \Phi \hat{\xi}(k-1) + \Gamma u_d(k-1). \quad (38)$$

Let  $\tilde{\xi}(k) = \xi(k) - \hat{\xi}(k)$ . It follows that

$$\tilde{\xi}(k+1) = (\Phi - L_c H \Phi) \tilde{\xi}(k). \quad (39)$$

For tuning simplicity, we place all the poles of the desired discrete ESO characteristic equation at  $-\beta$  where  $\beta = e^{-\omega_o T_s}$ .

Then the desired characteristic polynomial is

$$\lambda(z) = |zI - \Phi + L_c H \Phi| = (z - \beta)^3. \quad (40)$$

According to Ackermann's Formula [16], one has

$$L_c = \left( 1 - \beta^3, \frac{3(\beta-1)^2(\beta+1)}{2T_s}, -\frac{(\beta-1)^3}{T_s^2} \right)^T. \quad (41)$$

The discrete implementation of the control law (7) is

$$u_d(k) = \frac{\omega_c^2 [r - \hat{\xi}_1(k)] + 2\omega_c [\dot{r} - \hat{\xi}_2(k)] + \ddot{r} - \hat{\xi}_3(k)}{b}. \quad (42)$$

### C. Simulation Results

The key parameters of the vibrational MEMS gyroscope are  $\omega_n = 63881.1 \text{ rad/sec}$ ,  $\zeta = 0.0005$ , and  $\omega_{xy} = 6000 \text{ rad}^2/\text{sec}^2$ . The actual rotation rate is assumed to be  $0.1 \text{ rad/s}$ , and  $f_{\text{rate}} = 50 \text{ Hz}$ . The reference signal for the drive axis is  $r = A \cos(\omega t)$ , where  $\omega = 63428 \text{ rad/sec}$ . Typically the ideal output amplitude of the drive axis is  $A = 215 \text{ mV}$  for the piezoelectric vibration gyroscope. This voltage output is linearly related to the displacement output in micrometers. We use  $A = 215$  in "simulation units" to represent the magnitude of the drive axis output in the simulation. The output of the control signal is limited to  $\pm 100$ . In the simulation, the mechanical-thermal noise is applied and the PSD of mechanical-thermal noise is  $4.22 \times 10^{-2} \text{ N}^2/\text{sec}$ . The design parameter is  $b = k/m = 2.7178 \times 10^8$ . The controller bandwidth is  $\omega_c = 5 \times 10^5 \text{ rad/sec}$  and the observer bandwidth is  $\omega_o = 2.5 \times 10^6 \text{ rad/sec}$ . The sampling period is  $T_s = 1 \times 10^{-8} \text{ s}$ .

The output of the drive axis under the control of the discrete ADRC is shown in Fig. 3. After approximate  $2.2 \text{ ms}$ , the frequency of the drive axis is driven to the resonant frequency  $\omega$  as expected. Fig. 3 demonstrates the high tracking performance of the ADRC.

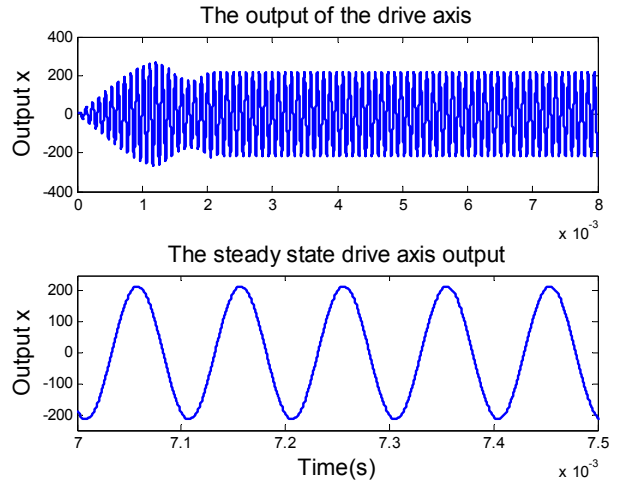


Fig. 3 The output of the drive axis with the ADRC.

To further investigate the robustness of the ADRC against parameter variations, the system parameters are changed as follows: the magnitude of the Quadrature error term, the damping coefficient, and the frequency of the rotation rate are increased by 10 times, i.e.,  $\omega_{xy} = 60000 \text{ rad}^2/\text{sec}^2$ ,  $\zeta = 0.005$ , and  $f_{\text{rate}} = 500 \text{ Hz}$ . With these plant parameter variations, the tracking error of the drive axis is shown in Fig. 4. Note that the tuning parameters in the ADRC keep the same as used in Fig. 3. It can be seen that the frequency of the drive axis is driven to the resonant

frequency  $\omega$  after approximate  $1.8ms$  and the steady state peak error between the reference and the drive axis output is around 0.17% of the desired amplitude. With the large scale plant parameter variations, the performance of the ADRC keeps almost the same. This shows the strong robustness of the ADRC.

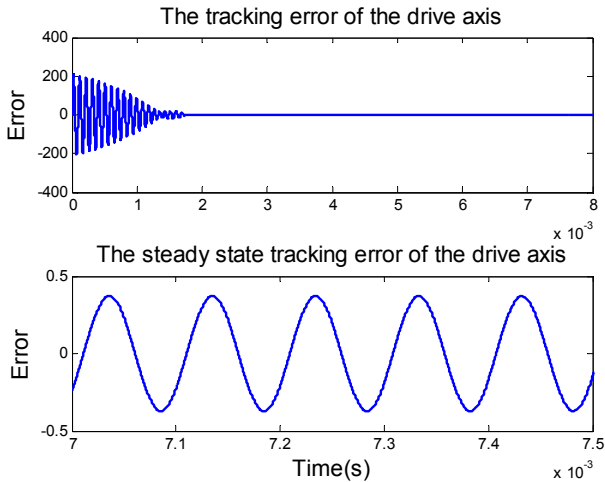


Fig. 4 The tracking error of the drive axis with parameter variations.

#### D. Hardware Test Results

The sampling period  $T_s=1 \times 10^{-8}s$  used in the simulation, however, is too fast to implement into the FPGA board, since the FPGA board clock speed is  $50 MHz$ , and the digital ADRC requires several clock cycles to process. For this reason, the tuning parameters are adjusted as the controller bandwidth is  $\omega_c = 2.5 \times 10^6 rad/sec$ , the observer bandwidth is  $\omega_o = 2.5 \times 10^6 rad/sec$ , and the sampling period is  $T_s = 1 \times 10^{-6} s$ . The output of the drive axis is shown in Fig. 5. From Fig. 5, it can be seen that the frequency of the drive axis is driven to the resonant frequency  $\omega$  after approximate  $18ms$ . At the steady state, the output matches the reference very well. The steady state peak error between the reference and the drive axis output is around 0.93% of the desired amplitude. These show the good performance of the ADRC in the FPGA implementation.

#### V. CONCLUSION

In this paper, a novel concept, active disturbance rejection, is successfully applied to solve the problems in MEMS gyroscopes that stem from manufacturing imperfections. Such imperfections manifest themselves as uncertain dynamics and unknown disturbances that are difficult to deal with using the existing design methods that are largely dependent on a good mathematical model. The proposed ADRC design proves to be a good fit for three reasons: 1) it requires minimal a priori information of the plant (just the order of the plant and its high frequency gain), 2) it actively estimates and compensates for the unknown dynamics and disturbances, 3) the controller is easy to implement and to tune, compared to other methods. The initial results in simulation and hardware tests are quite encouraging.

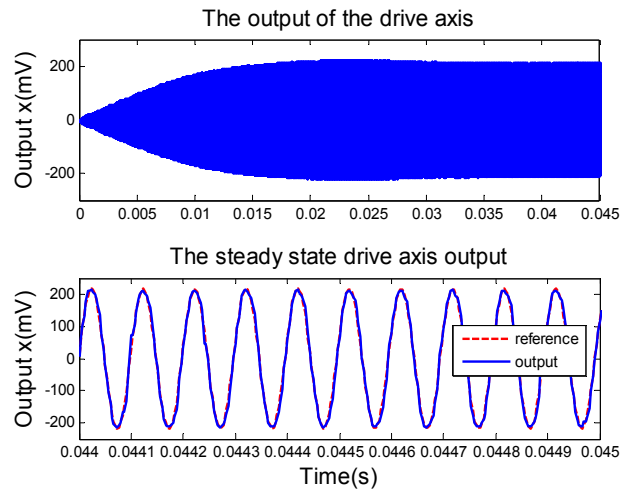


Fig. 5 The drive axis output of the FPGA implementation.

#### REFERENCES

- [1] Y. Yazdi, F. Ayazi, and K. Najafi, "Micromachined inertial sensors," *Proceedings of the IEEE*, vol. 86, no.8, pp.1640-1659, 1998.
- [2] R. P. Leland, "Adaptive tuning for vibrational gyroscopes," *IEEE Transactions On Control Systems Technology*, vol. 11, no. 2, pp. 242-247, 2003.
- [3] R. P. Leland, Y. Lipkin, and A. Highsmith, "Adaptive oscillator control for a vibrational gyroscope," *Proceedings of American Control Conference*, pp. 3347-3352, 2003.
- [4] R. T. M'Closkey, A. Vakakis, "Analysis of a micromsensor automatic gain control loop," *Proceedings of American Control Conference*, pp. 3307-3311, 1999.
- [5] L. Dong and R. P. Leland, "The adaptive control System of a MEMS gyroscope with time-varying rotation rate," *Proceedings of American Control Conference*, pp. 3592-3597, 2005.
- [6] R. Leland, "Lyapunov based adaptive control of a MEMS gyroscope," *proceedings of American Control Conference*, pp. 3765-3770, 2002.
- [7] S. Park, "Adaptive control strategies for MEMS gyroscopes," Ph.D. dissertation, University of California, Berkeley, 2000.
- [8] S. Park and R. Horowitz, "Adaptive control for the conventional mode of operation of MEMS gyroscopes," *Journal of Micro-electromechanical Systems*, vol.12, no.1, pp. 101-108, 2003.
- [9] Z. Gao, "Scaling and parameterization based controller tuning," *Proceedings of the American Control Conference*, pp. 4989-4996, 2003.
- [10] Z. Gao, "Active disturbance rejection control: a paradigm shift in feedback control system design," *Proceedings of the American Control Conference*, pp. 2399-2405, 2006.
- [11] Y. X. Su, B. Y. Duan, C. H. Zheng, Y. F. Zhang, G. D. chen, and J. W. Mi, "Disturbance-rejection high-precision motion control of a stewart platform," *IEEE Transactions on Control Systems Technology*, vol. 12, no. 3, pp. 364-374, 2004.
- [12] B. Sun and Z. Gao, "A DSP-based active disturbance rejection control design for a 1KW H-bridge DC-DC power converter," *IEEE Trans. on Industrial Electronics*, vol. 52, no. 5, pp. 1271-1277, 2005.
- [13] Q. Zheng and Z. Gao, "Motion control optimization: problem and solutions," *International Journal of Intelligent Control and Systems*, vol. 10, no. 4, pp. 269-276, 2006.
- [14] Z. Ping and Z. Gao, "A FPGA-based digital control and communication module for space power management and distribution systems," *In Proceedings of the American Control Conference*, pp. 4941-4945, 2006.
- [15] R. P. Leland, "Mechanical thermal noise in MEMS gyroscopes," *IEEE Sensors Journal*, vol. 5, no. 3, pp. 493-450, 2005.
- [16] G.F. Franklin, J.D. Powell, and M. Workman, *Digital Control of Dynamic Systems*, 3<sup>rd</sup> Ed., Addison-Wesley, 1997.